

Electronic Supplementary Information

Two-dimensional Ruthenium Boride: A Dirac Nodal Loop Quantum Electrocatalyst for Efficient Hydrogen Evolution Reaction

Zhen Gao,^a Fengxian Ma,^{a,*} Hongbo Wu,^a Yongheng Ge,^b Ziming Zhu,^b Ying Liu^a
Yalong Jiao,^{a,*} Zhongfang Chen^{c,*}

^a College of Physics, Hebei Key Laboratory of Photophysics Research and Application, Hebei Normal University, Shijiazhuang 050024, China

^b Key Laboratory of Low-Dimensional Quantum Structures and Quantum Control of Ministry of Education, Department of Physics and Synergetic Innovation Center for Quantum Effects and Applications, Hunan Normal University

^c Department of Chemistry, University of Puerto Rico, Rio Piedras Campus, San Juan, PR 00931, USA.

*E-mail:

fengxianma@hebtu.edu.cn;

yalong.jiao@hebtu.edu.cn;

zhongfang.chen1@upr.edu

Mechanical properties

To estimate the elastic limit of the RuB₄ monolayer, we investigated the stress-strain relation. As shown in Fig.S1, the RuB₄ sheet exhibits an anisotropic elastic response under uniaxial strain, and the ultimate strength along the x direction (13.86 N/m) is larger than that along the y direction (13.25N/m). The yield point along the x direction locates at $\varepsilon_x = -5\%$, indicating an irreversible plastic deformation when a larger compression is applied. The breaking point along x ($\varepsilon_x = 9\%$) is smaller than that along y ($\varepsilon_y = 17\%$), suggesting that the RuB₄ monolayer is relatively brittle along the x direction.

The curves of energy versus strain (Fig. S2) clearly show that the strain-free structure is in the equilibrium state. In elasticity theory, 2D Young's modulus along x and y directions are defined by the elastic constants as $Y_x^{2D} = (C_{11}C_{22} - C_{12}C_{21})/C_{22}$ and $Y_y^{2D} = (C_{11}C_{22} - C_{12}C_{21})/C_{11}$, respectively. The evaluated Y_x^{2D} and Y_y^{2D} values for the RuB₄ layer are 33.5 and 207.8 GPa · nm, respectively. The value of Y_y^{2D} is about 63% of that in 2D MoS₂ (330 GPa · nm),¹ but larger than that of phosphorene (23.0 - 92.3 GPa · nm).²

To explore the lattice response of the RuB₄ monolayer subject to deformation, we considered the uniaxial strain ε along x and y directions (Fig. S3). The values of

Poisson's ratio (PR) were calculated by the ratio of strain derivatives $\nu = -\frac{d\varepsilon_1}{d\varepsilon_2}$. As

shown in Fig. S3a and S3c, the in-plane resultant strain always decreases with increasing uniaxial strain, indicating that the in-plane PR of RuB₄ is positive.

Similarly, the thickness of the RuB₄ layer reduces under ε_y , giving rise to a positive

PR (Fig. S3d). Notably, when $+\varepsilon_x$ is applied (Fig. S3b), the thickness roughly decreases before $\varepsilon_x = 2\%$, implying a positive PR. When ε_x is greater than 2%, the thickness turns to increase, resulting in a negative PR. When $-\varepsilon_x$ is applied, a sign change of PR occurs at $\varepsilon_x = -2\%$. Note that a large PR value of -0.3 is estimated at $\varepsilon_x = 3\%$, greater than many reported monolayers, such as black phosphorus $(-0.027)^3$, silicon dioxides $(-0.022 \text{ to } -0.123)^4$, Be_5C_2 $(-0.041 \text{ to } -0.16)^5$ and borophane $(-0.053)^6$.

To understand the origin of negative PR in the RuB_4 sheet, we examined the evolutions of some key geometric parameters under different strains (Fig. S4). As shown in Fig. S4a, the unit cell of the sheet is comprised of two boron chains linked by transition metal atoms (Ru). The lattice constants (l_x and l_y) and the layer thickness

d are determined by: $l_x = l_1 + l_2$, $l_y = 4b_1 \sin(\frac{\theta_1}{2})$, and $d = b_2 \sin\theta_2$, respectively.

Here, b_2 is a B-B atom distance, and θ_2 is a dihedral angle (Fig. S4a, S4b). The thickness d is strongly related to the variation of θ_2 and b_2 . Note that l_1 and l_2 can be expressed by bond lengths and angles as well. The detailed analysis is given in Fig. S5.

Briefly, when $+\varepsilon_x$ is applied (Fig. S4c), b_2 decreases linearly with the increasing ε_x , while θ_2 gradually rises. The resultant d is slightly fluctuated, which is mainly attributed to the competition between b_2 and θ_2 . Overall, the change of θ_2 ($\Delta\theta_2$) is larger than that of b_2 . Therefore, $\Delta\theta_2$ is the dominant factor for the lattice response. An inflection point for d appears at $\varepsilon_x = 2\%$, where the $\Delta\theta_2$ slows down and Δb_2 overwhelms $\Delta\theta_2$. When $-\varepsilon_x$ is applied, the change of θ_2 is slow when $\varepsilon_x > -2\%$, but accelerates as $\varepsilon_x < -2\%$, leading to a positive PR to negative PR transition at -2% .

When ε_y is applied (Fig. S4e), the angle θ_2 decreases with the increase of ε_y , while the distance b_5 remains almost unchanged. Therefore, the thickness d follows the decreasing trend of θ_2 , and the PR is positive.

In short, the negative PR in the RuB₄ sheet is attributed to the competition between specific bond lengths and angles.

The Pourbaix diagram

The surface Pourbaix diagram for RuB₄ is constructed by plotting the most stable surface state under the relevant U_{SHE} and pH values. In our model, we assume that the oxidation of water to OH* and O* on RuB₄ lattice occur through the following steps:



Under standard conditions, the free energy of $\text{H}^+ + \text{e}^-$ is equal to $1/2 \text{H}_2$. Therefore, the above equations can be rewritten as:



The Gibbs free energies for reactions (3) and (4) are defined as ΔG_1^0 and ΔG_2^0 , respectively, and they are obtained by :

$$\Delta G^0 = \Delta E + \Delta E_{ZPE} - T\Delta S \quad (5)$$

where ΔE is the energy difference from reactions (3) and (4). The values from $E_{ZPE} - T\Delta S$ are calculated based on the values from ref. 7.

To include the effects of pH and potential U , we rewrite equation (5) as equations (6) and (7):

$$\Delta G_1 = \Delta G_1^0 - eU_{SHE} - k_b T \ln 10 \times pH \quad (6)$$

$$\Delta G_2 = \Delta G_2^0 - eU_{SHE} - k_b T \ln 10 \times pH \quad (7)$$

The free energy change of OH* and O* termination in Pourbaix diagram can be obtained as follows:

$$\Delta G_{OH^*} = \Delta G_1 \quad (8)$$

$$\Delta G_{O^*} = \Delta G_1 + \Delta G_2 \quad (9)$$

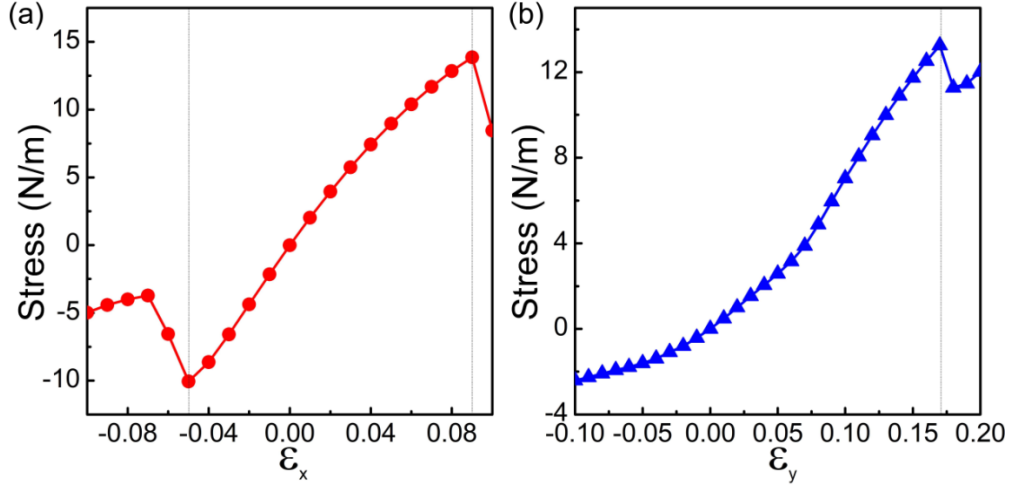


Figure S1. (a-b) Stress-strain curves for the RuB₄ monolayer along x and y directions.

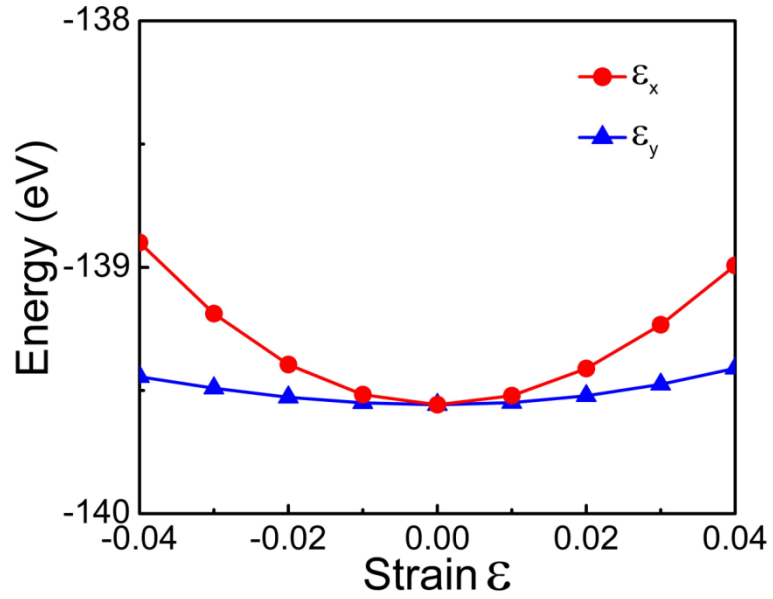


Figure S2. Energy-strain curves of the RuB₄ monolayer.

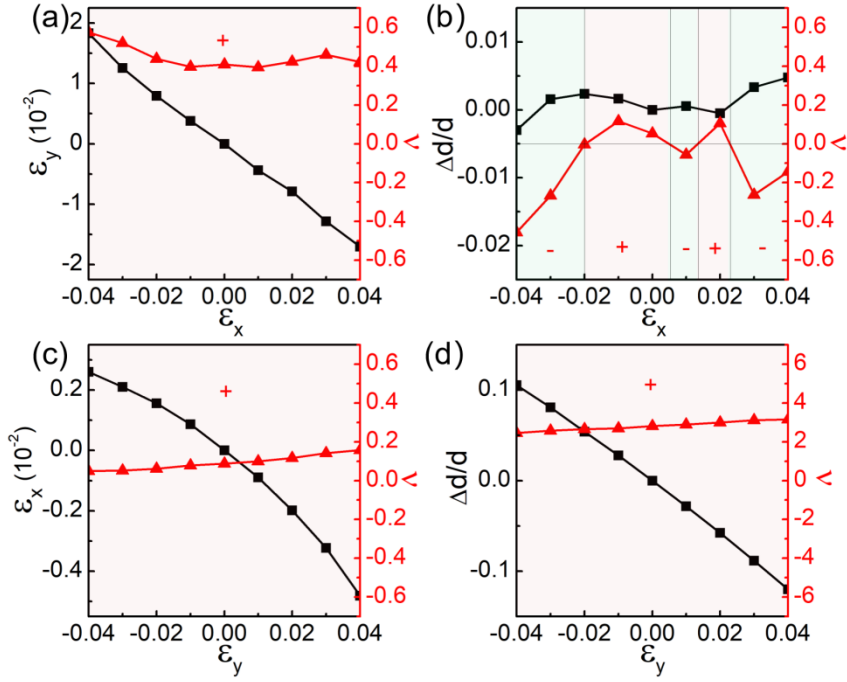


Figure S3. Mechanical response of the RuB₄ monolayer under the uniaxial strain along (a-b) *x* and (c-d) *y* directions. The light pink and blue region denote the Poisson's ratios (PR) with positive (+) and negative (-).

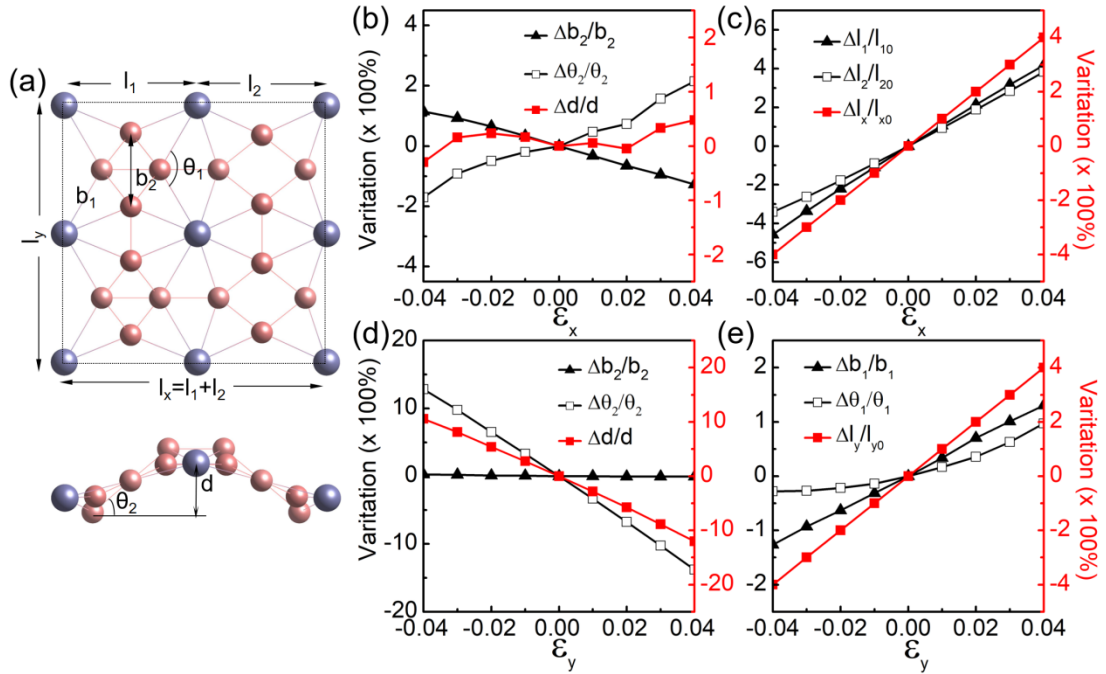


Figure S4. (a) Top and side views of the RuB₄ unit cell. The thickness *d* is governed by the dihedral angle θ_2 and the distance between the specific B atoms (*b*₂). (c-d) The evolution of the structural parameters (*b*₂, θ_2 , *d*) of the RuB₄ monolayer under strains

along x direction. The thickness d was obtained through the equation $d = b_2 \sin \theta_2$. (d-

e) The variation of the structural parameters (b_2 , θ_2 , d) of the RuB₄ monolayer under strains along y direction. The lattice vector lengths l_x and l_y were obtained through

$$l_x = l_1 + l_2 \text{ and } l_y = 4b_1 \sin\left(\frac{\theta_1}{2}\right), \text{ respectively.}$$

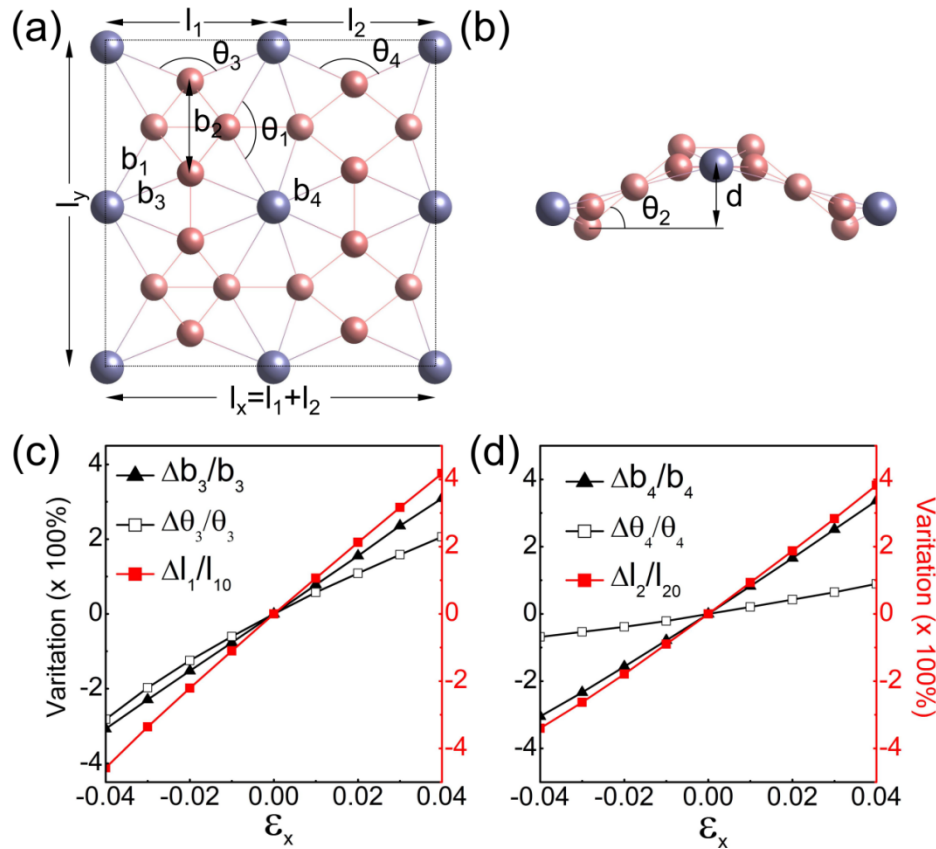


Figure S5. (a-b) Top and side views of the RuB₄ monolayer. Two lattice vectors in the rectangular cell are directly related to the distance between Ru atoms. (c-d) Dependence of the bonding parameters b_3 , b_4 , θ_3 , and θ_4 on the strain along x and y directions (ϵ_x and ϵ_y) of The length l_1 , and l_2 were obtained through equation

$$l_1 = 2b_3 \sin\left(\frac{\theta_3}{2}\right), \text{ and } l_2 = 2b_4 \sin\left(\frac{\theta_4}{2}\right), \text{ respectively.}$$

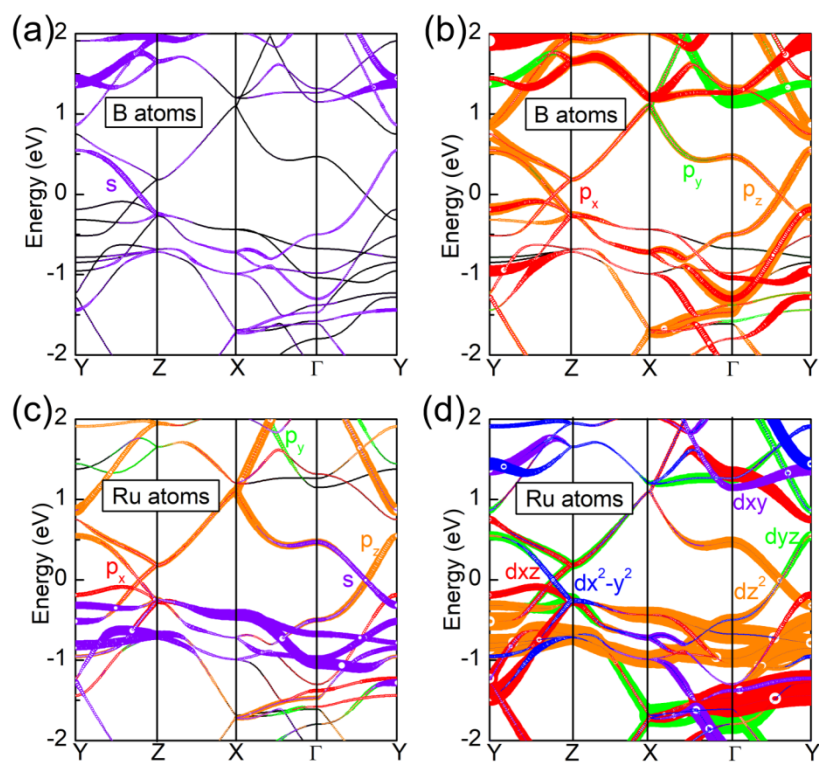


Figure S6. Orbital-resolved band structures for the RuB₄ monolayer.

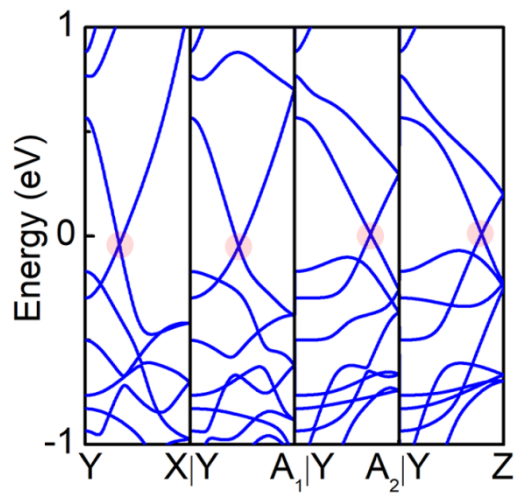


Figure S7. Band structure of the RuB₄ monolayer along selected band paths illustrated in Figure 3c.

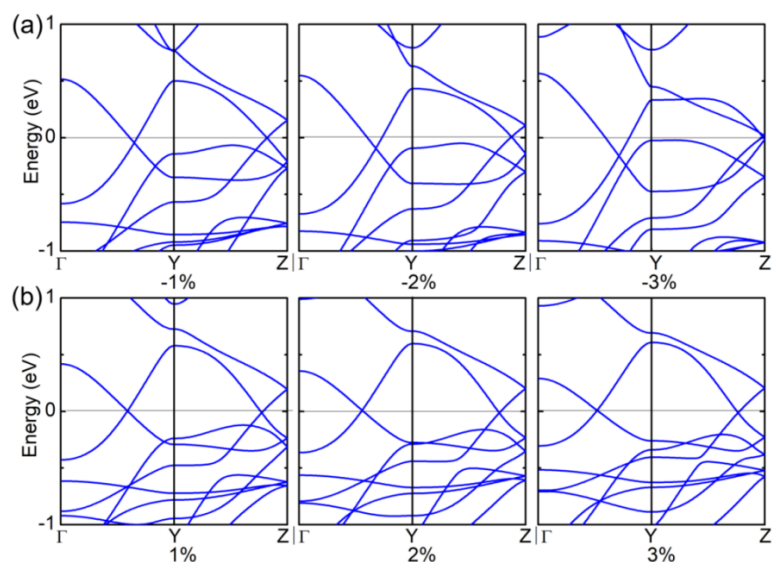


Figure S8. Band structure of the RuB₄ monolayer under (a) compressive and (b) tensile biaxial strains. The Fermi level was set to zero.

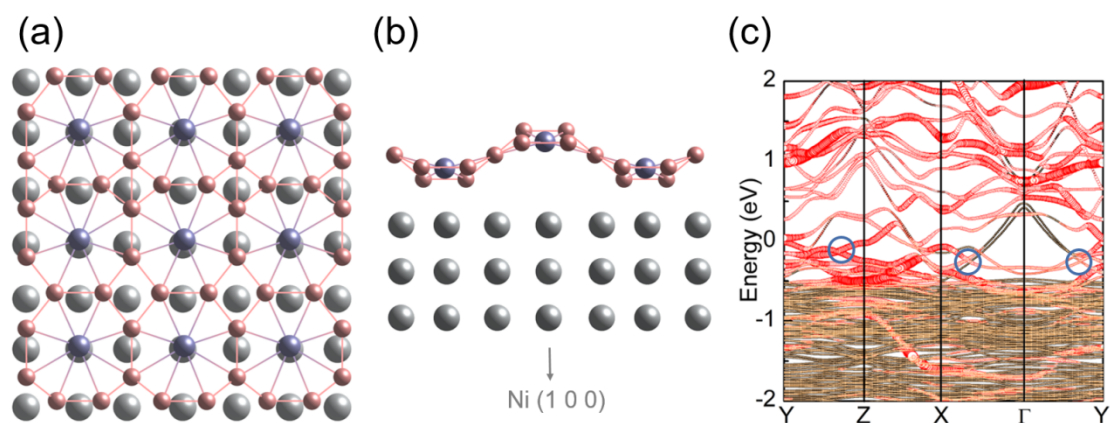


Figure S9. (a-b) Top and side view of the RuB₄+Ni (1 0 0) system. (c) The corresponding band structure (spin up channel) for RuB₄+Ni (1 0 0) system. Red and orange lines indicate the band contribution from RuB₄ and Ni element, respectively.

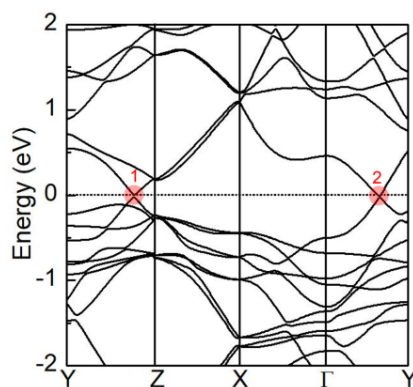


Figure S10. Band structure of the RuB₄ monolayer by the PBE+U+SOC method.

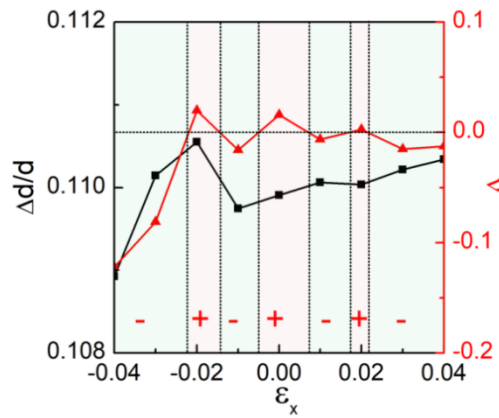


Figure S11. Mechanical response of hydrogen adsorbed RuB₄ monolayer under uniaxial strain x . The light pink and blue region denote the Poisson's ratios (PR) with positive (+) and negative values (-).

In **Figure S11**, we further found that hydrogen adsorption does not bring any significant effect on the mechanical response under strain effects, thus the auxetic property of the RuB₄ monolayer can be preserved upon hydrogen adsorption.

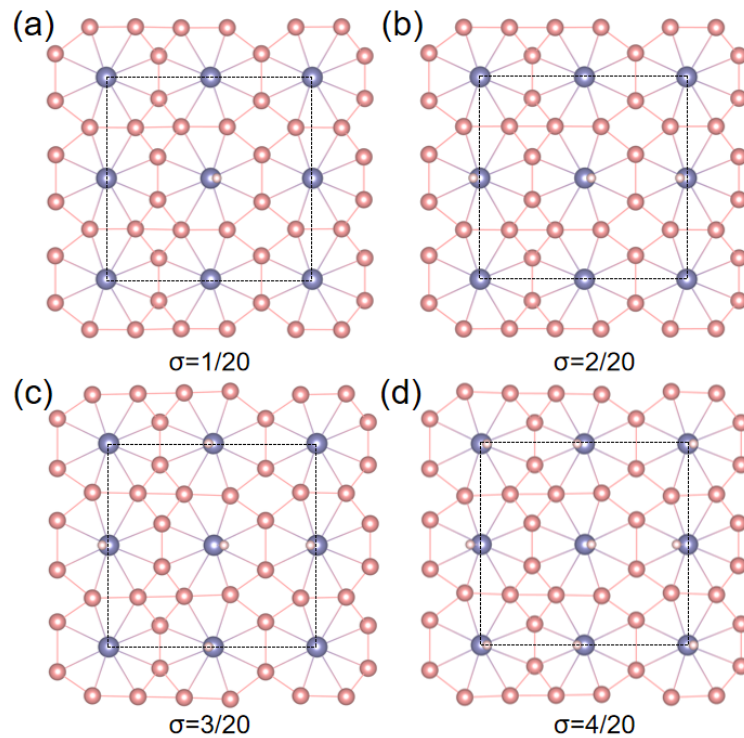


Figure S12. Illustration of stable adsorption states with different hydrogen coverage.

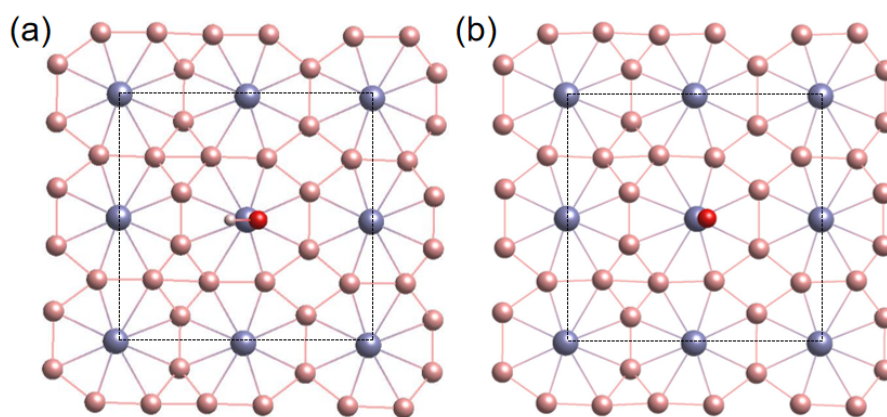


Figure S13. Structural configurations of (a) OH and (b) O adsorbed RuB₄ sheets.

Table S1. The elastic constants (in GPa•nm) for the RuB₄ monolayer.

C_{11}	C_{22}	C_{66}	C_{12}
34.52	214.1	82.98	14.79

References

1. A. Castellanos-Gomez, M. Poot, G. A. Steele, H. S. J. van der Zant, N. Agrait and G. Rubio-Bollinger, *Adv. Mater.*, 2012, **24**, 772-775.
2. L. Wang, A. Kutana, X. Zou and B. I. Yakobson, *Nanoscale*, 2015, **7**, 9746-9751.
3. J.-W. Jiang and H. S. Park, *Nat. Commun.*, 2014, **5**, 4727.
4. Z. Gao, X. Dong, N. Li and J. Ren, *Nano Lett.*, 2017, **17**, 772-777.
5. Y. Wang, F. Li, Y. Li and Z. Chen, *Nat. Commun.*, 2016, **7**, 11488.
6. L. Kou, Y. Ma, C. Tang, Z. Sun, A. Du and C. Chen, *Nano Lett.*, 2016, **16**, 7910-7914.
7. Á. Valdés, Z. W. Qu, G. J. Kroes, J. Rossmeisl and J. K. Nørskov, *The Journal of Physical Chemistry C*, 2008, **112**, 9872-9879.